A uniplanar three-axis gradient set for *in vivo* magnetic resonance microscopy

Andrey V. Demyanenko, Lin Zhao, Yun Kee, Shuyi Nie, Scott E. Fraser, J. Michael Tyszka *

Division of Biology, California Institute of Technology, 2A Broad 114-96, 1200 E California Blvd., Pasadena, CA 91125, USA

A B S T R A C T

We present an optimized uniplanar magnetic resonance gradient design specifically tailored for MR imaging applications in developmental biology and histology. Uniplanar gradient designs sacrifice gradient uniformity for high gradient efficiency and slew rate, and are attractive for surface imaging applications where open access from one side of the sample is required. However, decreasing the size of the uniplanar gradient set presents several unique engineering challenges, particularly for heat dissipation and thermal insulation of the sample from gradient heating. We demonstrate a new three-axis, target-field optimized uniplanar gradient coil design that combines efficient cooling and insulation to significantly reduce sample heating at sample-gradient distances of less than 5 mm. The instrument is designed for microscopy in horizontal bore magnets. Empirical gradient current efficiencies in the prototype coils lie between 3.75 G/cm/A and 4.5 G/cm/A with current and heating-limited maximum gradient strengths between 235 G/cm and 450 G/cm at a 2% duty cycle. The uniplanar gradient prototype is demonstrated with non-linearity corrections for both high-resolution structural imaging of tissue slices and for long time-course imaging of live, developing amphibian embryos in a horizontal bore 7 T magnet.

© 2009 Elsevier Inc. All rights reserved.

1. Introduction

Magnetic resonance microscopy (MRM) has proven useful in a wide range of biological imaging applications requiring spatial resolutions on the order of 10–100 μm [1–4]. There is increasing interest in high-resolution MRM of millimeter scale samples such as developing embryos [5–10] and for non-invasive histology of entire organisms, organs or tissue samples [11–14].

Most successful MRM studies to date have employed radiofrequency and gradient coils with a cylindrical geometry and large coil filling-factors for both coils, closely surrounding the sample in order to maximize the signal-to-noise ratio (SNR) of the image and the efficiency of gradient generation. While minimizing coil size improves SNR efficiency, it also imposes significant constraints on mounting, access and environmental control of the sample during the experiment.

The importance of controlling resistance and associated heating in small gradient coils has been discussed in detail for cylindrical gradient sets [15]. When combined with fabrication limits on inter-track gaps and conductor cross-sectional area, the issue of heating control dominates all MR microscopy gradient designs. Additionally, for *in vivo* applications, it is imperative that the organism be thermally insulated from the gradient set which may exhibit temperature rises during normal operation of many 10s of degrees centigrade.

Uniplanar gradient designs represent an underexploited alternative to cylindrical gradients improving access to the sample, allowing larger medium volumes for better environmental control, and enabling MRM of superficial regions within a larger organism. The development of a compact uniplanar gradient set with good thermal insulation and heat dissipation was originally motivated by time-lapse imaging of models of early vertebrate development, specifically externally developing amphibian embryos [6] or cultured mouse embryos [16]. The uniplanar design allows the gradient and RF coil hardware to be placed extremely close (less than 5 mm and 1 mm, respectively) to the sample with a corresponding increase in signal detection sensitivity and gradient current efficiency. In most MR microscopy applications, gradient hardware capable of generating field gradients of many hundreds of G/cm is highly advantageous for imaging small samples at high spatial resolution without compromising minimum sequence timing parameters. This provides a clear motivation for developing a uniplanar gradient set without the spatial constraints of high performance cylindrical designs [15]. Although it is markedly more difficult to design uniplanar sets with large regions of gradient uniformity, this is offset by significantly relaxed constraints on total sample size and access. The stage geometry allows unobstructed optical access to the sample from above, with the potential for simultaneous high numerical aperture optical imaging and deep tissue magnetic resonance imaging.

Relatively few designs for planar gradients have been reported [17–22], with most designs representing biplanar gradi-

* Corresponding author. Fax: +1 626 395 2000.
  E-mail address: jmt@caltech.edu (J.M. Tyszka).

ent sets appropriate for open human MRI systems employing a pair of permanent magnet pole pieces with the main field oriented vertically [17,18,20]. Optimized biplanar coil windings for finite areas and minimum inductance have been reported using methods such as stream function representation of current density that are also applicable to uniplanar gradient geometries. Uniplanar or surface gradient coil designs [23–28] have not received as much attention since cylindrical or biplanar gradient coils meet the requirements of most applications and avoid some of the design and operational complexities inherent in uniplanar designs. Dodd and Ho describe both uniplanar and biplanar microscopy gradient designs with discrete wire concentric return paths intended for very high resolution imaging of small samples [29]. These coils were capable of extremely high gradient efficiencies (on the order of 100 G/cm/A) and could achieve spatial resolutions in oil phantoms between 6 μm and 8 μm. However, despite describing water cooling as imperative for this design, no cooling system was implemented and *in vivo* imaging was not demonstrated. Lemdiasov and Ludwig recently introduced a finite-element formalism for design of generalized surface gradient coils which allows for more complex current surface geometries and demonstrates a continued interest in these designs [30]. More recently, Aksel et al. demonstrated a three-axis uniplanar gradient design for human imaging applications with a 16 cm uniform region and 0.14 G/cm/A efficiency [23]. Their use of the target field method and distributed uniplanar coil winding designs is similar to the approach described here, though at a far larger scale. The design described here also differs from larger uniplanar designs in terms of more stringent thermal insulation and cooling requirements resulting from the small dimensions of the instrument.

We describe here the design, fabrication and initial testing of a uniplanar gradient set intended for use within a horizontal bore high field magnet with thermal insulation and heat dissipation sufficient to allow long time-series MRM of living samples.

2. Materials and methods

All imaging was performed using a 7 T, 30 cm diameter horizontal bore Bruker Avance 300 imaging spectrometer (Bruker Biospin, Billerica, MA). The MR microscope hardware consisted of a planar RF coil, three-axis uniplanar gradient module, a water-cooled heat exchange, air cooling manifold and a stage frame (Fig. 1). The instrument was designed to fit within the 120 mm internal diameter of a commercial cylindrical gradient set (Model S116, Bruker Biospin) that physically supported the uniplanar hardware but was otherwise disabled during uniplanar imaging. This arrangement allowed convenient switching between the S116 and uniplanar gradients as required. Commercial gradient amplifiers (Modified Copley Model 265, Bruker Biospin GmbH, Germany) were used to drive the uniplanar microscope gradient coils. Shimming was achieved using DC offsets to the uniplanar gradient currents and second order terms provided commercial room temperature shims present outside the S116 gradient set. For the samples and RF coil described below, conventional iterative minimization of the observed sample linewidth was found to converge effectively despite the non-uniformity of the uniplanar gradient fields. The design and fabrication of each uniplanar microscope component is described in detail below.

2.1. Radiofrequency coils

The MR stage microscope geometry favors RF coil designs with extended horizontal and limited vertical coverage. For the initial prototype, a planar loop coil with a mean diameter of 6.9 mm (inner diameter 5.6 mm, outer diameter 8.2 mm) was etched from copper laminate with a 0.9 mm thick FR4 substrate and mounted within the air cooling manifold on the stage surface (Fig. 4). The tune and match circuit was placed above the stage but close to the loop due to space limitations between the RF coil and gradient module. Samples were placed asymmetrically within 35 mm Petri dishes and manually positioned over the RF coil center. The center
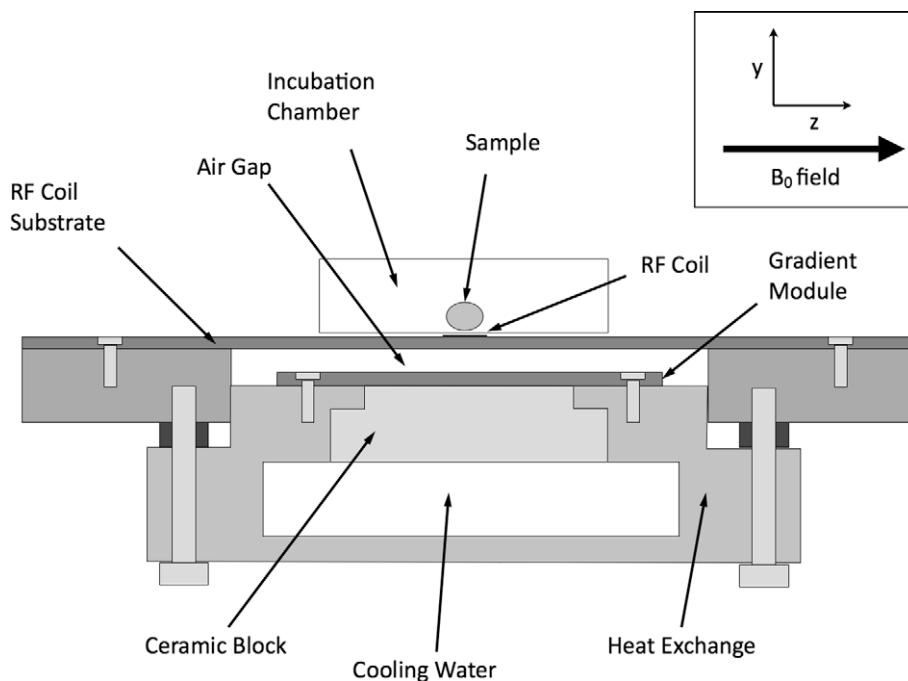

Fig. 1. Cross-section schematic of the prototype microscope stage showing the relation between sample incubator, RF coil, insulating air gap, gradient coil module, ceramic heat exchange and cooling water. Active cooling of the gradient module and effective insulation of the sample from gradient module heating are critical if the stage microscope is to be used for *in vivo* imaging. The x dimension is perpendicular to the page with the y dimension normal to the gradient and RF coil planes.

axes of the RF and gradient coils were accurately coregistered by the air manifold and stage frame.

2.1.1. Uniplanar gradient coil design

Design approaches for planar gradients are based typically on a vector stream function description of a uniplanar or biplanar current density [18,19,21]. The current density itself can be derived either analytically or numerically from the desired field for each gradient axis, although numerical optimization offers more flexibility for optimized design of finite size gradients with multiple component cost functions. The planar current density in an ideal gradient coil is represented as the curl of a vector stream function, $\mathbf{S}(\mathbf{r})$

$$\mathbf{J}(\mathbf{r}) = \nabla \times \mathbf{S}(\mathbf{r}) \tag{1}$$

Since the current density is restricted to a plane at $y = 0$ and $\mathbf{J}_y(\mathbf{r}) = 0$ for all values of $\mathbf{r}$, it follows that $\mathbf{S}_x(\mathbf{r}) = 0$ and $\mathbf{S}_z(\mathbf{r}) = 0$ for all values of $\mathbf{r}$ and the vector stream function can be expressed in terms of a scalar function, $\phi(x,z)$ at $y = 0$, as follows:

$$\mathbf{S}(\mathbf{r}) = \phi(x,z)\hat{\mathbf{y}} \tag{2}$$

The magnetic vector potential generated by a planar current density is given by:

$$\mathbf{A}(\mathbf{r}) = \frac{\mu_0}{4\pi} \int d^3\mathbf{r}' \frac{\mathbf{J}(\mathbf{r}')}{|\mathbf{r} - \mathbf{r}'|} \tag{3}$$

allowing numerical calculation of the magnetic field as the curl of the magnetic vector potential

$$\mathbf{B}(\mathbf{r}) = \nabla \times \mathbf{A}(\mathbf{r}) \tag{4}$$

For computational efficiency, the discretized form of the scalar stream function, ϕ_{xz}, was calculated as the outer product of two discrete piecewise cubic hermite polynomials (PCHIPs) [31]. Unlike

cubic splines, PCHIPs preserve monotonicity in the interpolation, reducing the complexity of the final winding pattern. Vectors, q_i and r_i, corresponding to the x and z dimensions of the stream function, were constructed from a combination of fixed boundary values and optimizable free values, c_j. For a y gradient with two free parameters per dimension, we have

$$\begin{aligned} q_i &= \{\, 0 \quad c_1 \quad c_2 \quad 0 \quad -c_2 \quad -c_1 \quad 0 \,\} \\ r_i &= \{\, 0 \quad c_3 \quad c_4 \quad c_4 \quad c_3 \quad 0 \,\} \end{aligned} \tag{5}$$

Discrete PCHIPs, $\mathbf{P_x}$ and $\mathbf{P_z}$, typically 32 elements in length were interpolated from q_i and r_i and the discrete scalar stream function over the finite current plane constructed as the outer product of $\mathbf{P_x}$ and $\mathbf{P_z}$.

$$\phi_{xz} = \mathbf{P}_x^T \mathbf{P}_z \tag{6}$$

This process is illustrated for four free parameters per PCHIP in Fig. 3. Computational efficiency was maintained by field optimization over the target volume surface only, using the approach originally suggested by Turner et al. for cylindrical gradient coil design [32]. An additional B_z offset parameter was included in the optimization to compensate for the inherent field offset of the y gradient at the center of the target volume. Various optimization cost functions were explored and the discrete form shown in Eq. (7) was chosen for the optimization of the first prototype gradient coil designs:

$$\begin{aligned} F(\phi_{xz}) = {}& \alpha \sum_{k,l} (\mathbf{B}_z(k,l) - \mathbf{B}_z^{\mathrm{targ}}(k,l))^2 \\ &+ \beta \sum_{m,n} \left[\left(\frac{\Delta_m \phi(m,n)}{\Delta m} \right)^2 + \left(\frac{\Delta_n \phi(m,n)}{\Delta n} \right)^2 \right] \end{aligned} \tag{7}$$

Here, integers k and l index the surface of the ellipsoidal volume of uniformity (Fig. 2a), m and n index the finite current plane at $y = 0$.
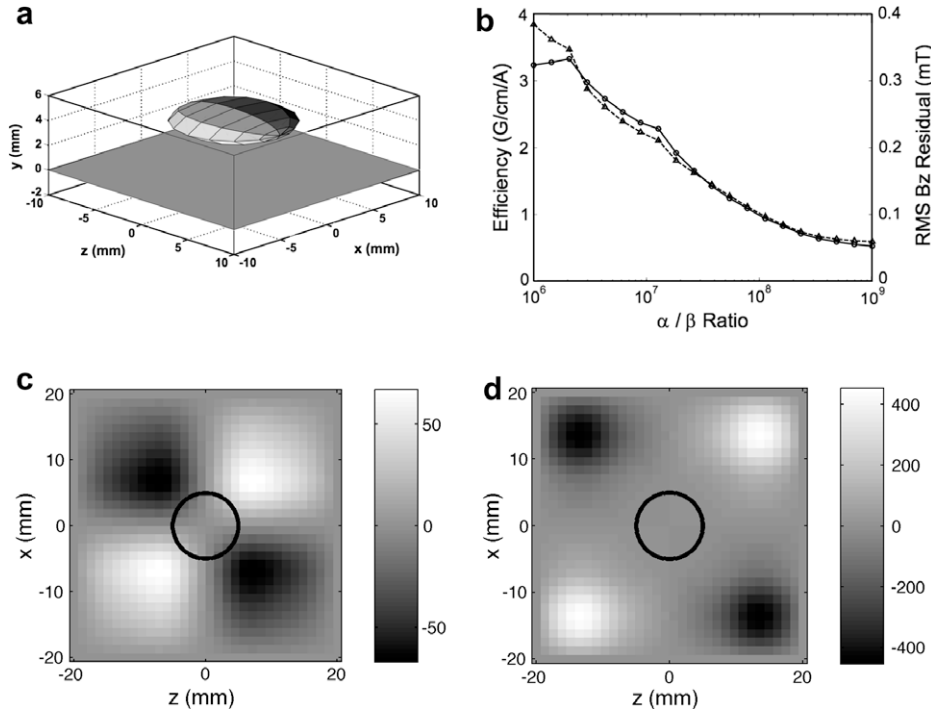

Fig. 2. (a) Visualization of the ellipsoidal target volume used for planar gradient current density optimization. The target B_z field for an x field gradient is shown projected onto the ellipsoid. The target volume has 5 mm semi-major axes in x and z and a 1 mm semi-minor axis in y. (b) The tradeoff between the RMS residual field on the target volume (dashed line, triangles) and the current efficiency (solid line, circles) is shown for an example x gradient coil design. (c) Efficiency-weighted stream function design ($\alpha/\beta = 10^6$) with current density concentrated close to the coil center. (d) Uniformity-weighted stream function design ($\alpha/\beta = 10^9$) with current density concentrated away from the coil center.

$\Delta_m/\Delta m$ represents the finite difference estimate of the local stream function gradient in the dimension indexed by m. The weights α and β allow the uniformity of the generated magnetic field gradient to be balanced against minimum conductor spacing in the final winding pattern as represented by the gradient of the stream function. Penalization of the stream function gradient forces current density to be more evenly distributed within the current plane, resulting in higher efficiency gradient generation at the expense of gradient uniformity (Fig. 2b). For the first prototype, the cost function weights were balanced empirically, with large α/β ratios (Table 1) emphasizing efficiency over gradient uniformity (Fig. 2c and d). This cost function has not been previously described for gradient design, and represents one of many possible functions. Additional terms representing design parameters such as stored energy [21], inductance [30], and torque [30] could be added to address future requirements.

The final fabricated design was generated from the stream function in Fig. 2c with an α/β ratio of 10^6 on a 40 mm × 40 mm current plane. The target volume had a major axis of 10 mm $x–z$ and minor axis of 2 mm in y, and was offset by 4.5 mm from the current plane (Fig. 2a).

2.2. Gradient coil fabrication

By convention, the current winding pattern for each coil axis is derived from equally spaced contours of the scalar stream function [33]. Photoresist masks for the upper and lower layers of each gradient coil were generated from the optimized discrete stream function using a combination of custom-written Matlab functions and a commercial CAD package (Solidworks, Concord, MA). The front and back artwork was chemically etched into double-sided 70 μm thick copper laminate on a 160 μm thick Arlon91 substrate. This process is comparable to milling approaches in solid copper [15,23] except that the small scale of the gradients allows chemical etching.

The front and back gradient conductor planes were connected by soldering at the center of each spiral section allowing a continuous path through the conductor pattern with input and output leads only at the periphery. Gradient conductor layers were electrically insulated from each other with 160 μm thick Arlon91 film and potted into a single module using thermally conductive epoxy resin (Duralco 128, Cotronics Corporation, Brooklyn, NY). The final gradient order was set by resistive heating considerations as X (closest to heat exchange), Z, Y (closest to sample). Gradient conductors were connected to the MR system gradient amplifiers by air-cooled heavy gage (16 AWG) copper wiring.

Table 1
Design and performance parameters for the three-axis uniplanar gradient set. Empirical efficiency was estimated from uniformity phantom images in the region indicated in Fig. 7.

Gradient axis	Resistance (Ω)	Turns	α/β	Temperature coefficient (°C/W)	Modeled efficiency (G/cm/A)	Empirical efficiency (G/cm/A)
X	0.60	5	10^6	0.36	3.57	4.09
Y	0.15	3	10^4	1.13	3.67	4.48
Z	0.32	6	10^6	0.64	2.35	3.75

2.3. Water cooled heat exchange

An active cooling system for the gradient conductors has been developed and constructed specifically for the uniplanar gradient module. The design consists of a heat exchange consisting of a lower baffled reservoir containing flowing chilled water coupled to the gradient module by a high thermal conductivity, electrically insulating ceramic (Shapal-M®, Goodfellow Corporation, Oakdale, PA) (Fig. 1).

Thermal testing of the gradient coil module was performed to assess the efficiency of water cooling and air cooling/insulation using both constant and pulsed currents.

The temperature rise on the surface of each gradient was calibrated against input power using a DC power supply (BK Precision 1670A I_{max} = 3.3 A), with the gradient module and water cooling heat exchange assembled but not mounted in the stage frame, chilled water (11–12 °C) was provided by a commercial water heater/chiller (VWR Scientific Model 1160). The temperature variation on the upper surface of the gradient module, closest to the sample stage, was measured using a calibrated copper-constantan T-type thermocouple (Omega Engineering Inc., Stamford, CT) with a Biopac amplifier and AcqKnowledge software (Biopac Systems, Inc., Goleta, CA).

Gradient surface temperature rises were also measured using gradient pulse trains generated by the MR imaging gradient amplifiers at a 4% duty cycle (10 ms pulse duration, 250 ms repetition time) and peak instantaneous currents ranging from 7.5 to 45 A. Current pulsing was continued for between 200 and 300 s to capture the kinetic and equilibrium temperature response. Cooling water at 11–12 °C was supplied by the commercial high volume re-circulating water chiller (Neslab Merlin M75, Thermo Scientific, Newington, NH).
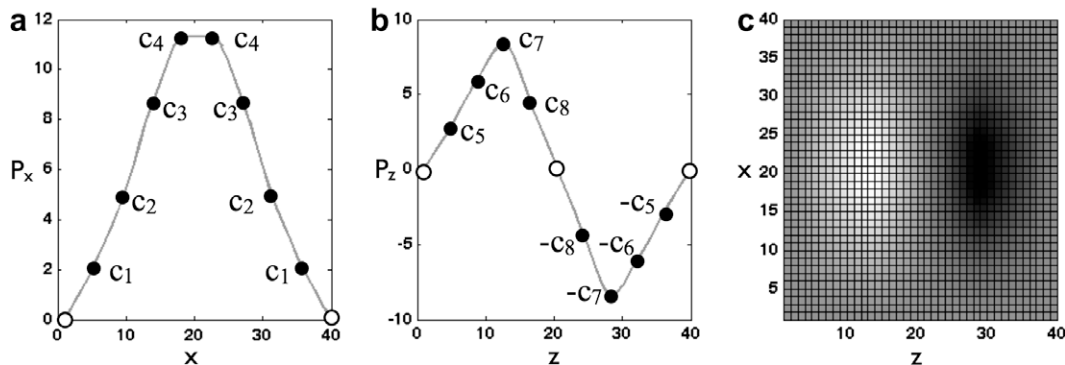

Fig. 3. Use of piecewise cubic hermite interpolating polynomials (PCHIPs) to construct (a) P_x and (b) P_z from vectors q_i and r_i which in turn are constructed from symmetric or antisymmetric combinations of the free parameters parameters c_i (solid circles) and boundary conditions represented by fixed elements of q_i and r_i (open circles). The outer product of P_x and P_z generates the discrete stream function ϕ_{xz} for the planar current density (c). The PCHIPs and stream function generated by four free parameters per dimension are shown.

2.4. Thermal insulation and air cooling

Target organisms such as mammalian and amphibian embryos require accurate temperature control during imaging. Water cooling of the gradient set through the ceramic block and heat exchange described above does not provide complete protection of the sample from gradient heating in some cases. An air cooling manifold was constructed (Fig. 4d) which channeled compressed, room temperature air both around the sample container and below the RF coil, between the coil substrate and the gradient module. Protection of the sample from gradient heating is therefore achieved by a combination of active and passive insulation. Air flowing through the 1 mm gap between the lower surface of the RF coil substrate and the upper surface of the gradient module provides active cooling if necessary. The 0.9 mm thick RF coil substrate provides a second layer of passive thermal insulation. Total insulation effectiveness was assessed using thermocouple measurements (as above) during gradient pulsing on each axis.

2.5. Support frame

The purpose of the stage frame is to provide rigid support for both the electronic components (RF coils, gradient coils, etc.) and for the sample within an incubation chamber. The frame was fabricated from materials that would not interact significantly with the polarizing magnetic field of the magnet, including plastics, resins, glass, ceramics and non-ferromagnetic metals (Fig. 4e). The stage allows accurate positioning of the MR hardware (gradient and RF coils) within the homogeneous volume of the magnet and of the sample at the isocenter of the gradient and RF coils. The stage was centered within the magnet bore using a set of small, constrained wheels placed at the edge of the circular end-plates of the stage frame.

2.6. Demonstration imaging

All demonstration imaging was performed using a 7 T 30 cm horizontal bore Bruker Avance imaging spectrometer (Bruker Biospec, Billerica, MA) using either the uniplanar gradient insert or conventional cylindrical gradients.

A uniformity phantom was constructed to allow experimental estimation of the gradient efficiency within the designed target volume. The phantom consisted of an approximately 8 mm × 8 mm × 16 mm block of polyetherimide plastic, into which were drilled an orthogonal array of 750 μm holes under CNC control. The holes had a center-to-center spacing of 2.13 mm in x, 1.19 mm in y and 1.19 mm in z based on reference images acquired using a cylindrical gradient set. The block was submerged in a 5 mM gadoteridol solution and imaged using a volumetric FLASH sequence (TR/TE = 50 ms/ 2.2 ms, 4 averages, voxel size within target volume = 75 μm). The resulting images were zero padded by a factor of two and a spatial Hamming filter applied to minimize ringing artifacts.

An approximately 2 mm thick coronal slice of a perfusion fixed C57BL/6 mouse brain was isolated and soaked in 2.5 mM gadoteridol in phosphate buffered saline and 0.01% sodium azide for two hours and imaged using a 3 D FLASH imaging sequence with the following parameters: TR/TE = 75/4.0 ms, isotropic voxel size in target volume 36 μm, matrix size = 192 × 192 × 80, 16 averages, total imaging time 5 h 7 min. RF excitation gain was adjusted for maximum total signal using the FLASH sequence.

Developing embryos of the African Clawed Frog (*Xenopus laevis*) were obtained by fertilization of oocytes harvested using standard procedures [34]. The embryos were imaged during normal development for 15 h at room temperature. Sequential 3D multiple gradient echo (MGE) images were acquired using the following parameters: TR/TE = 275/1.9,4.8,7.7,10.7 ms, estimated isotropic voxel size in target volume 76 μm, matrix size = 160 × 160 × 40, 1 average, total imaging time per volume 29 min 20 s. RF excitation gain was adjusted for maximum total signal using the MGE sequence. All four echo images were averaged to improve SNR forming a single, predominantly T2*-weighted volume image at each time point.

Chemical fixation and live embryo imaging were performed according to protocols approved by the Internal Animal Care and Use Committees of the California Institute of Technology and the University of California, San Diego.
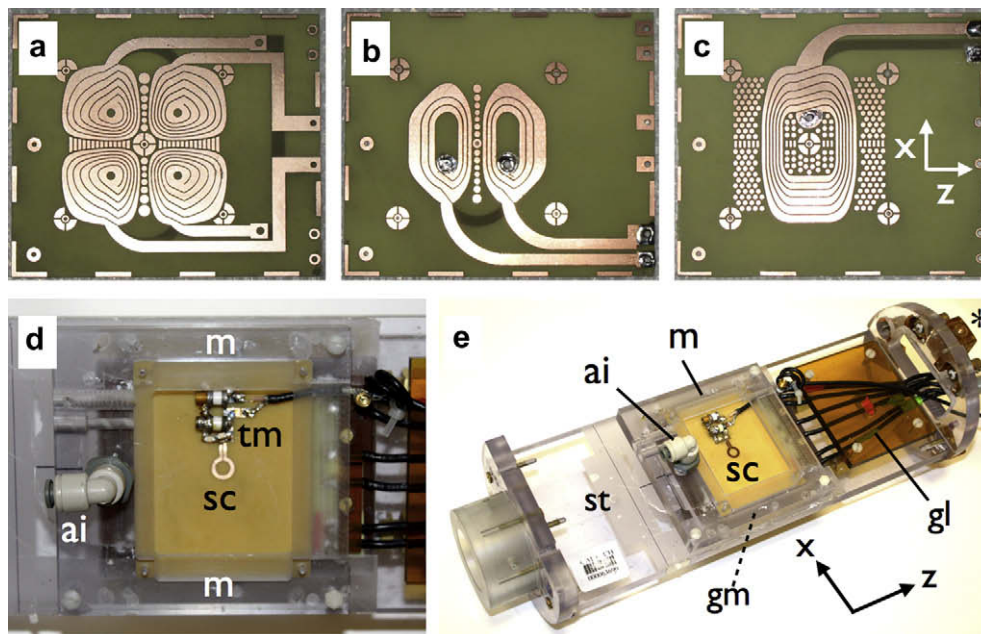

Fig. 4. Fabricated MR microscope stage components. Etched upper layer conductor patterns for the (a) *X*, (b) *Y* and (c) *Z* gradient coils. (d) Plan view of the air cooling manifold mounted over the single turn 6.9 mm RF transceiver surface coil. (e) View of the assembled MR microscope stage insert from above. *Abbreviations:* ai, manifold air intake; m, air cooling manifold; sc, RF surface coil; tm, tune and match circuit; st, stage frame; gm, gradient module (beneath stage); gl, gradient leads. *x* and *z* axes are indicated in (c) and (e) for reference.

2.7. Gradient non-uniformity correction

Gradient non-uniformity is difficult to control in uniplanar gradient sets. A variety of geometric distortion corrections have been suggested [17,23], typically involving the calculation or measurement of the B_z field across the imaging volume and an associated nonlinear transformation of the acquired image. For the uniplanar gradients described here, distortion correction was achieved using an approach similar to that described in Aksel et al. [23] using numerically simulated fields accounting for the dual-layer design and extended to three dimensions. Given a location in reconstruction space (x,y,z) and simulated fields for each gradient axis (B_z^x, B_z^y, B_z^z), for a given nominal linear gradient within the target volume (G_x, G_y, G_z) we estimate the corresponding position (x',y',z') in the distorted image as:

$$x' = \frac{B_z^x(x,y,z)}{G_x}$$
$$y' = \frac{B_z^y(x,y,z)}{G_y} \qquad (8)$$
$$z' = \frac{B_z^z(x,y,z)}{G_z}$$

The geometrically corrected volume image was then reconstructed by applying the transform defined by Eq. (8) with tricubic interpolation to the warped images. Correction for the spatial modulation of signal intensity due to voxel size changes arising from gradient non-linearity was achieved by calculation of the local Jacobian determinant of the transformation [35].

3. Results

3.1. Gradient coil design

Optimization of the planar current density for each gradient axis was relatively efficient with typical convergence in 12–55 iterations (approximately 80–325 cost function evaluations) for a 10×10 sample target field ellipsoid and a 32×32 current density matrix and fractional convergence tolerance of 10^{-6}.

The optimization typically completes in 1–2 min on a modern 64-bit workstation. The use of cost function weights to balance gradient current efficiency against field linearity was effective, though the two weights used here could potentially be replaced by a single weight with appropriate normalization of the cost function components. The trade-off between accuracy and efficiency is demonstrated in Fig. 2. As α/β increases, the field generated by the optimal current density more closely matches the target field but current density is weighted more towards the periphery of the coil, resulting in lower gradient current efficiency.

The B_z field and associated field gradient for each coil are shown in Fig. 5. Fields were simulated numerically from Biot-Savart simulation of the discrete elements of the stream function contours used to fabricate the final coil. This approach allowed the number of winding turns to be simulated explicitly. The non-linearity of the resulting gradient fields is visualized both as the percent deviation of the magnitude of the gradient from the ideal gradient and in terms of the gradient direction in Fig. 5b. The 5% contour of the absolute value of this deviation is also shown, providing a a visual indicator of the volume within which the gradient field is relatively uniform. The X coil is the least linear, with a central volume of uniformity approximately 4 mm across in x–z and 0.5 mm in y. The Y coil is very linear in x–z over 10 mm and linear over 1 mm in y. The z coil is linear over more than 10 mm in x and y, but only over 2 mm in z. Together the coils provide a volume of gradient uniformity to within 5% approximately 4 mm × 0.5 mm × 2 mm in x, y and z, respectively.

3.2. Gradient current efficiency

The design and efficiency parameters of the fabricated uniplanar gradient coils are summarized in Table 1. The gradient current efficiencies in G/cm/A were estimated from the imaged hole spacing within the region of interest indicated in Fig. 7, corresponding to the approximate location of the target volume. It should be noted that the gradient efficiency varies spatially and that all voxel resolutions are estimated at the center of the target volume.
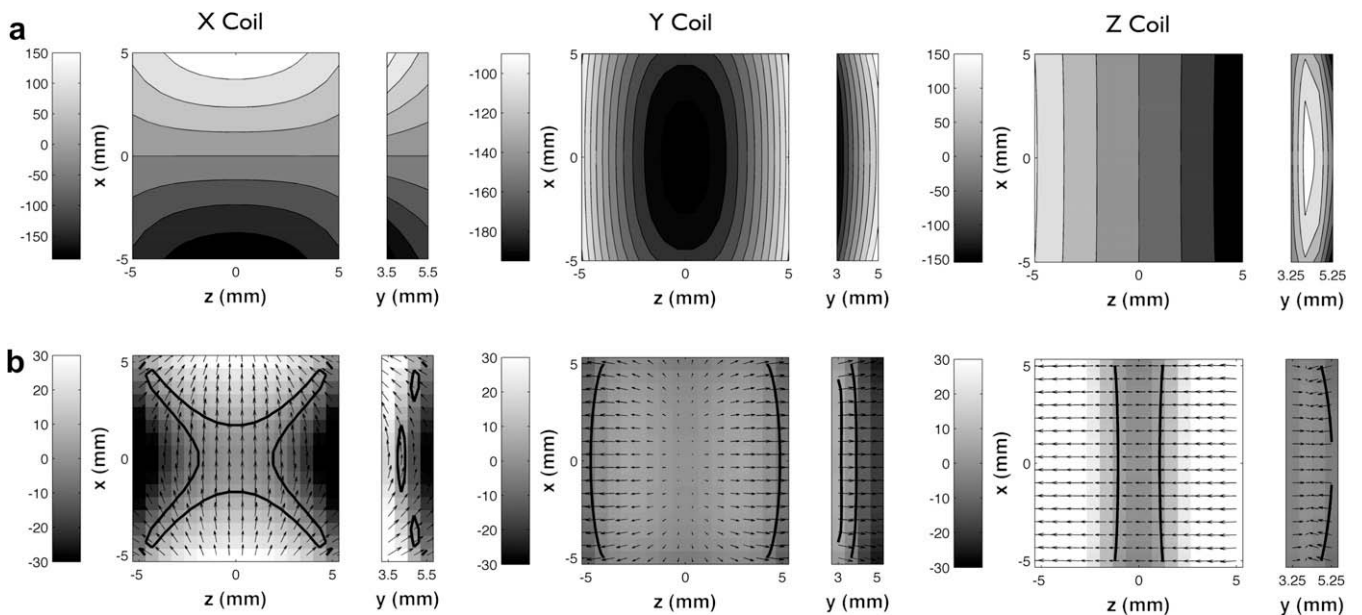

Fig. 5. Simulated magnetic field and field gradient uniformity plots at 1 A current (see Table 1 for α/β ratios and turns). (a) xz and xy sections through the generated B_z field (in μT) at the center of the target volume for each gradient axis. (b) Field gradient direction (arrows) overlaid on the deviation of the gradient amplitude from the ideal gradient (in percent). The 5% contour for the absolute deviation from ideal is shown for each coil.

3.3. Thermal testing

Thermal performance testing was performed using a full-size gradient module with continuous water cooling at 11–12 °C. The temperature rise was observed to be linear with input power for DC currents ranging from 0 to 3.3 A (Fig. 6a). The measured thermal response coefficient, C_T, for each gradient axis is reported in Table 1. The typical temporal evolution of the gradient surface temperature is shown in Fig. 6b. The temperature rise and decay at the gradient module surface following the start and end of current pulsing were modeled as monoexponential processes. Characteristic time constants for temperature rise and decay were calculated as $\tau_R = 4.78 \pm 0.52$ s and $\tau_D = 4.47 \pm 0.44$ s, respectively. Equilibrium temperature rises on the gradient module surface in response to 4% duty cycle pulsing of the Y coil at currents of 22.5 A, 30 A and 45 A were 2.5 °C, 5 °C and 12 °C, respectively (Fig. 6b). Thermal response coefficients reflected the arrangement of gradient coils in the module, with the Y gradient possessing the largest coefficient due to its proximity to the thermocouple and distance from the heat exchange.

3.4. Air cooling and insulation

Air cooling tests were performed using the assembled uniplanar gradient and RF coil with the air manifold in place (Fig. 4). A typical imaging load was simulated using a continuous 7.5 A current applied to the Y coil for 6 min, equivalent to a constant field gradient of 33.6 G/cm. Temperature was recorded using a thermocouple placed on the upper surface of the RF coil. In the absence of air flow, the RF coil surface temperature rose by approximately 0.62 °C (Fig. 6c). With room temperature airflow at a calibrated 42 L/min, the temperature rise reduced to 0.22 °C. The temperature of the surface of the Y coil rose approximately 11 °C. Without airflow, the time constants of the temperature rise and decay were 57 ± 2 s and 63 ± 3 s, respectively. With airflow, the time constants fell to 31 ± 2 s and 32 ± 2 s, respectively. Although not implemented in this prototype, thermostatically controlled airflow would further reduce any residual temperature increase at the stage surface and would also allow experiments under conditions other than room temperature.

3.5. Maximum gradient strength estimation

The balance of resistive heating in a given gradient coil against heat dissipation via water cooling, airflow and other means results in maximum equilibrium temperature rises at the gradient module surface and RF coil as discussed in Section 3.3. The relation between the gradient surface temperature rise, ΔT, and the generated field gradient, G, can be derived as:

$$\begin{aligned}\Delta T &= C_T \langle P \rangle \\ &= C_T I^2 R D \\ &= C_T (G/\eta)^2 R D\end{aligned} \tag{9}$$

where C_T is the thermal response coefficient (in °C/W), R is the coil resistance (in ohms), D is the duty cycle, and η is the gradient current efficiency (in G/cm/A). The gradient associated with a maximum allowable temperature rise is then

$$G_{max} = \eta \sqrt{\frac{\delta T_{max}}{C_T R D}} \tag{10}$$
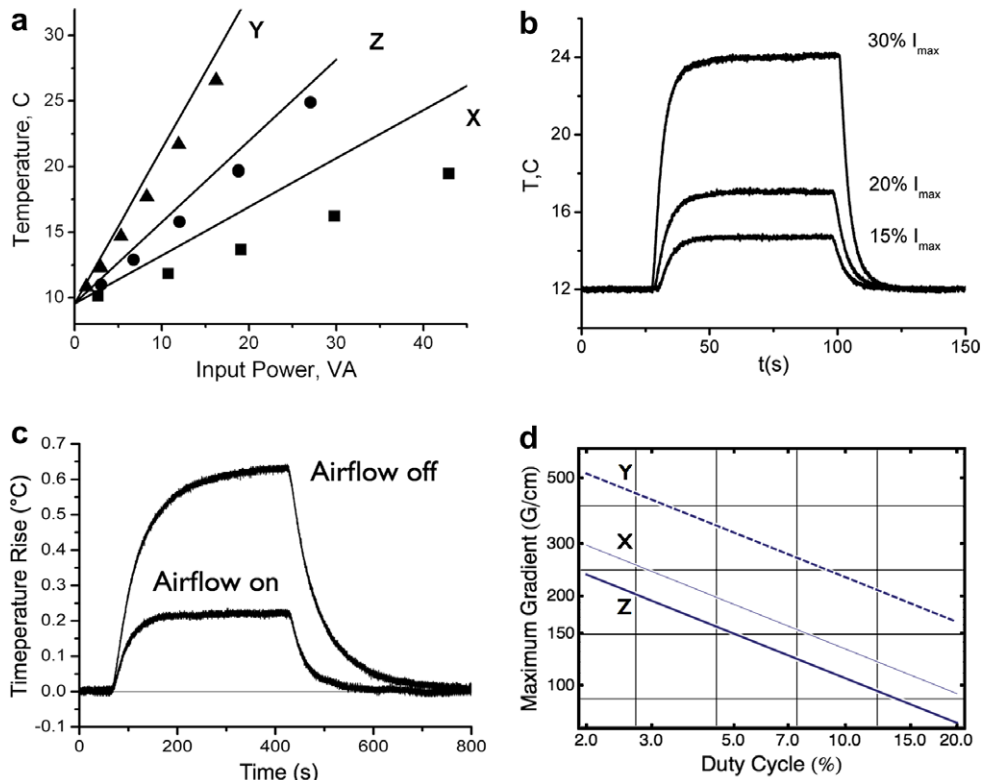

Fig. 6. Resistive heating effects for uniplanar gradient set with constant water cooling. (a) Surface temperature (measured by calibrated thermocouple) versus input power for the X, Y and Z gradient coils. Pulsed current measurements are indicated by discrete symbols, DC current measurements by solid regression lines for each axis. (b) Temperature response of the gradient set to a 10 ms pulse every 250 ms (4% duty cycle) at currents of 15% (22.5 A), 20% (30 A) and 30% (45 A) of I_{max} (150 A). (c) Impact of sub-stage airflow on the observed temperature rise at the stage surface. (d) Variation of the maximum predicted gradient strength with duty cycle for each axis assuming a maximum allowable temperature increase of 40 °C at the gradient module surface.

Using 40 °C as a working limit on allowable surface temperature rise for the gradient module, we can estimate the corresponding maximum gradient as a function of pulse duty cycle for each coil axis using the empirical coefficients and resistances with modeled efficiencies shown in Table 1. The results are graphed in Fig. 6d, with maximum gradients of 236 G/cm (X), 517 G/cm (Y) and 296 G/cm (Z) at 2% duty cycle and 75 G/cm (X), 164 G/cm (Y) and 94 G/cm (Z) at 20% duty cycle. In practice, currents would also be limited to 100 A on any given axis to avoid fusing, resulting in combined current- and heating-limited maximum gradients of 236 G/cm (X), 448 G/cm (Y) and 296 G/cm (Z) at 2% duty cycle.

3.6. Demonstration imaging

Images of the uniformity phantom demonstrate the severe geometric distortion expected with uniplanar designs which is most pronounced in the y dimension perpendicular to the gradient plane (Fig. 7). Distortion correction based on field simulations was found to be highly effective at restoring geometric integrity. The increase in voxel size with distance from the gradient in the original image appears as increased blurring with distance from the gradient. Although the impact on point spread function of the image is uncorrectable, the modulation of signal intensity can be corrected successfully by Jacobian determinant scaling, resulting in images which appear very similar to those acquired using the large diameter cylindrical gradient set (for example Fig. 7a and c). Without Jacobian correction, the increase in point spread function approximately balances the decrease in coil sensitivity in y, resulting in an almost uniform signal intensity in the reconstructed uniplanar images (Fig. 7d and h).

High resolution structural images of the mouse brain slice reconstructed at an isotropic 39 μm grid (original target volume resolution 37 μm) clearly visualized major myelinated white matter structures including the internal and external capsule, hippocampal commisure and fimbria (Fig. 8). The slice was sufficiently thin to avoid the most extreme distortion effects seen in the uniformity phantom. The short tissue T_1 resulting from soaking in gadoteridol allows for high SNR efficiency while preserving strong gray-white matter contrast in this T2*-weighted image.

Volumetric MGE imaging of developing frog embryos was demonstrated successfully for a 15 h time-series at room temperature (Fig. 9). Active air cooling was not required for this experiment although active air-temperature control would allow for modulation of developmental rate in the embryos [5]. The formation of the blastocele (a central fluid space within the early embryo) provided a valuable marker for normal development, allowing identification of slowly or abnormally developing embryos. Averaging of multiple gradient echoes to form a single mixed contrast image provided a valuable boost in SNR while maintaining tissue contrast within the embryo and preserving temporal resolution compared to a single-echo sequence. Previous work suggests that the bioeffects of MRI in developing frog embryos are minimal [5,6,36]. Further refinement of the environmental control system, particularly with regards to thermostatic air-flow, would be essential for developmental biology experiments.

4. Discussion

Uniplanar gradient sets are not without significant limitations, and it is not expected that they would be considered for general purpose use in MRM. In addition to the loss of geometric integrity, the gradient field non-uniformity makes quantitative diffusion imaging difficult over larger volumes, even with accurate field calibration. For applications where gradient uniformity is essential, biplanar designs offer similar advantages to the uniplanar design
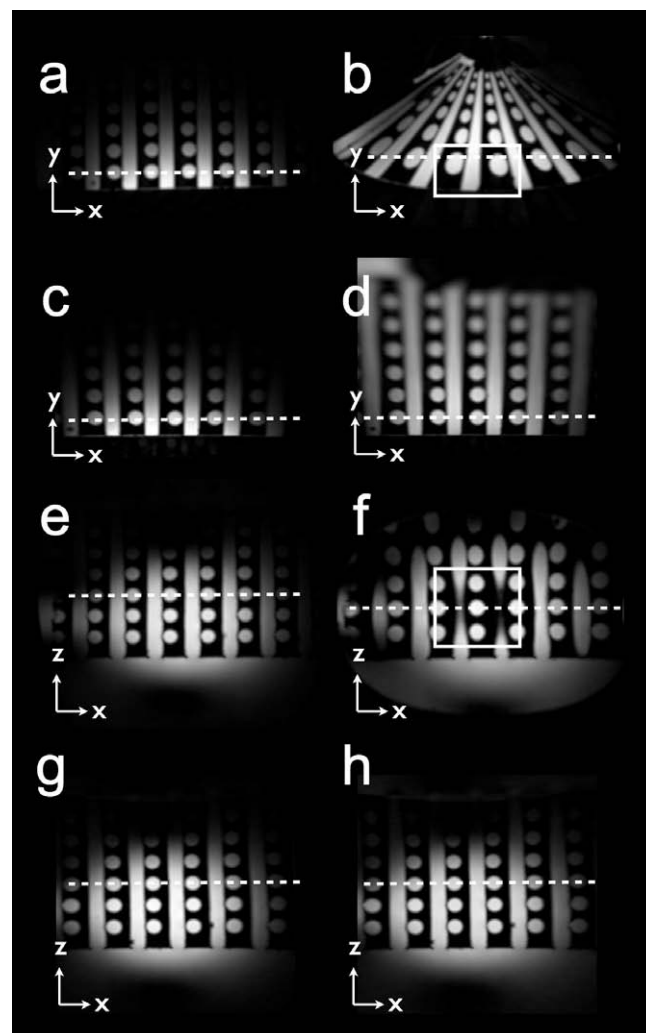

Fig. 7. Correction of geometric distortion due to gradient nonlinearity. Reference images acquired using a 120 mm internal diameter cylindrical gradient set of a uniformity phantom (a and e). Uncorrected uniplanar gradient images of the same phantom (b and f). Distortion corrected images with Jacobian determinant scaling (c and g) can be compared directly with the reference images (a and e) and demonstrate the accuracy of the correction. Distortion correction without Jacobian determinant scaling (d and h) reveals the expected increase in spatial blurring with distance from the gradient as the effective voxel size increases. The location of the corresponding x–z slice (e–h) is indicated in each x–y slice (a and d) and vise versa, is indicated by a dashed line. The region used for empirical gradient efficiency estimation is shown as a solid rectangle.

at the expense of access and sample size restrictions for equivalent gradient efficiencies. However, the same advantages that make the uniplanar instrument attractive for developmental biology may also be relevant for non-biological MR microscopy in porous media, process chemistry and materials science.

Geometric correction of structural biological images acquired with the uniplanar gradient set is essential, particularly for comparison with stained histological sections, standard atlases and for volumetric and morphological studies. Although the use of the simulated gradient field proved very effective, further improvements are possible. For example, a more accurate simulated field could be generated by finite element modeling of the full conductor design, including connector leads. Alternatively, an empirical calibration of the generated field based on a more finely structured uniformity phantom would likely prove most accurate, and is the approach favored by most manufacturers of clinical MRI systems [37].
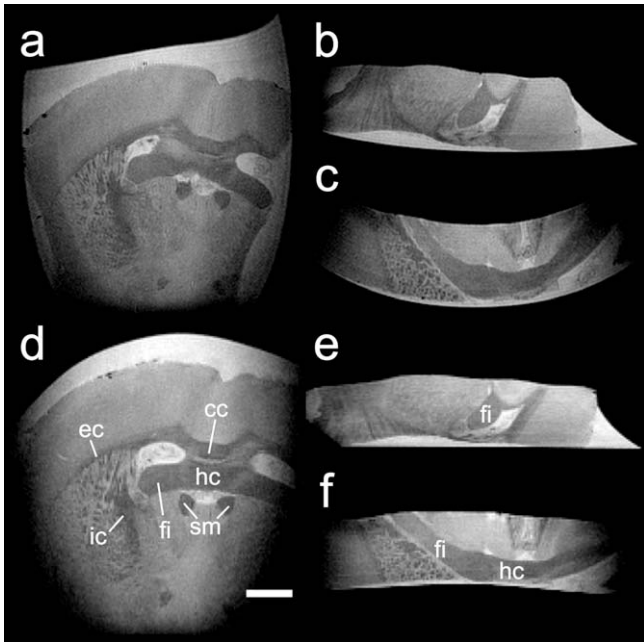
Fig. 8. Volumetric imaging of an approximately 2 mm thick coronal slice from a perfusion fixed C57BL/6 mouse brain soaked in 5 mM gadoteridol imaged with the uniplanar gradient set. Sections in the z–x (a and d), x–y (b and e) and z–y planes (horizontal–vertical) are shown for uncorrected (a–c) and distortion corrected (d–f) data. A variety of myelinated structures are visualized, including the internal capsule (ic), external capsule (ec), hippocampal commisure (hc), stria medullaris (sm), corpus callosum and fimbria (fi). Uncorrected images (a)–(c) demonstrate the pronounced geometric distortion associated with the gradient non-uniformities of a uniplanar gradient set. Geometric correction using the numerically modeled gradient field greatly reduces the distortion (d)–(f). The reconstructed voxel size in (d)–(f) is 39 μm, scale bar = 1 mm.

The gradient efficiency of our design does not match the performance of previously reported planar microscopy designs, largely due to the emphasis placed here on practical *in vivo* applications. For example, Seeber et al. achieved gradient strengths exceeding 15 T/m and efficiencies in excess of 10 G/cm/A with a biplanar design tailored for solenoidal microcoil imaging [38]. However the duty cycle at maximum gradient strength was limited to 0.1% with air cooling, making it unlikely that it would find application for rapid *in vivo* imaging of millimeter scale organisms. Similarly, the air-cooled uniplanar micrococpy design reported by Dodd and chien [39] achieved gradient efficiencies of 35, 90 and 110 G/cm/A for *X*, *Y* and *Z* coils, respectively, but was demonstrated in oil phantoms only. An additional cooling system was recommended but not implemented, again making *in vivo* application unlikely.

Performance comparisons between uniplanar and cylindrical gradient designs of similar size are less valuable, since each geometry addresses different application needs. If the finite current plane of a uniplanar gradient is wrapped around a cylinder, the cylindrical geometry will generate a far more linear field gradient with a higher efficiency, but at the expense of maximum sample size. As an example, a commercial cylindrical microimaging gradient available at the time of writing (Model Micro5, Bruker Biospin, Billerica, MA) has a gradient efficiency of 4.8 G/cm/A, in internal diameter of 19 mm and a maximum RF coil diameter of 10 mm, with a presumably smaller maximum sample size.

The uniplanar gradient set was originally motivated by environmental control issues associated with imaging live developing embryos at high spatiotemporal resolution. Previous MRI studies of developing frog embryos were performed at either 11.7 T or 14 T using solenoidal RF coils and either one or two embryos per time-series [5,36,40]. In such studies, the individual spatial resolution and sensitivity were very high, but there was little guarantee that the selected embryos would develop successfully during the
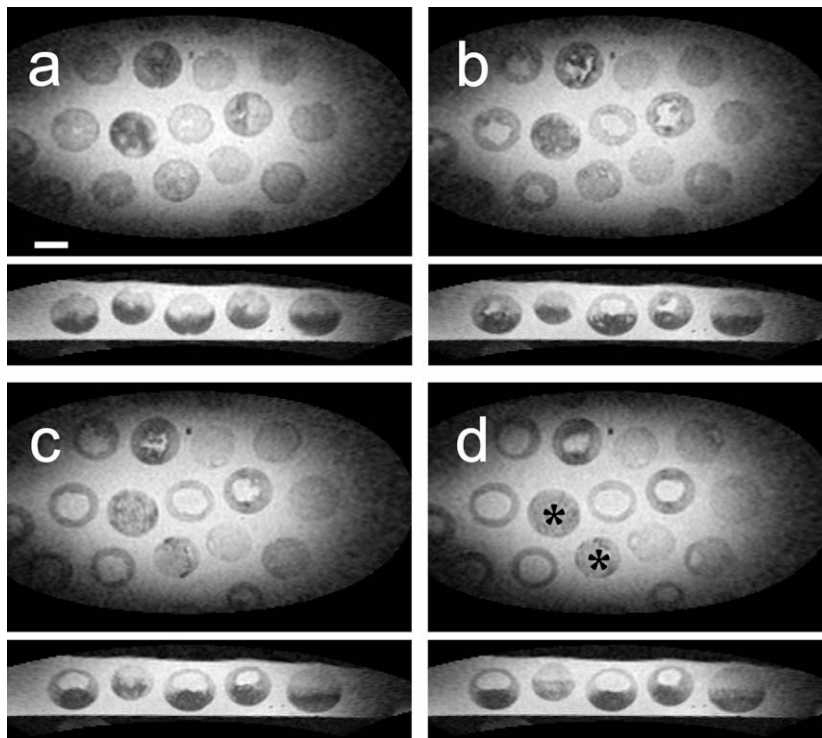

Fig. 9. Four of 30 volumetric images from a serial study of live developing *Xenopus laevis* embryos acquired using the uniplanar gradient set. x–z (above) and x–y (below) sections are shown at experimental times of (a) 0:00 h (b) 3:30 h (c) 7:30 h and (d) 11:30 h. Images have been corrected for geometric distortion without intensity correction. Tissue contrast between dark, lipid-rich vegetal cells and lighter animal cells are apparent in the x–y sections. Abnormally or slowly developing embryos are easily identified (examples indicated by asterisk in d). The formation of the blastocele can be followed in the majority of embryos (asterisks). Volumes were reconstructed with an isotropic voxel size of 47 μm from an original nominal voxel size at the center of the FOV of 76 μm. Imaging time per volume was 29 mins 20 s. Scale bar in (a): 1 mm.

experiment. Imaging a group of embryos, as demonstrated here, significantly increases the chances of observing at least one successful development. The uniplanar gradient is well suited geometrically to imaging groups of embryos arranged in a Petri dish, incubation chamber or well-plate, where the samples are dispersed in the *x*–*z* plane but do not extend far in the *y* dimension. *In vivo* optical imaging of deep embryonic tissues in developmental model organisms is often restricted by tissue opacity, providing an opportunity for MRM to provide complementary structural imaging data beyond the scope of optical methods. As the embryo grows, it becomes increasingly difficult to obtain high quality images from deeper structures. The MR stage microscope is also well suited to studies of cultured mouse embryos, due to the ease with which the open stage design accommodates additional environmental control systems, and the strengths of MRI in opaque soft tissue imaging, particularly when combined with rapid image acquisition techniques such as echo planar imaging that fully exploit the uniplanar gradient performance.

Another promising application area would be for high spatial or temporal-resolution imaging of superficial structures in animal models such as the mouse, which are much larger than the gradient set. Historically, this reasoning has been the primary motivation for the development of uniplanar or surface gradient coils for human imaging [23,27]. Imaging of the full thickness (approximately 2 mm, Fig. 8d) of the dorsal cortex of the mouse brain may be feasible using this uniplanar gradient set with the mouse lying supine on the stage. Likewise, the uniplanar gradient has some potential for *in utero* imaging of developing mouse fetuses, which lie superficially in the abdomen of the mother. The high gradient efficiency and fast switching speed of the uniplanar gradient are particularly valuable when physiological motion, both from the mother and fetus can be pronounced. In both these application areas, high gradient strengths can be achieved without severely constraining access to the mouse for physiological and anesthesia support.

Although not discussed in detail here, the uniplanar gradient design would have some advantages over biplanar and cylindrical gradients for dual-mode optical-MR microscopy. Open access to the sample from above provides more flexibility for optics and light path design than previous dual-mode instruments such as the MR-confocal microscope described by Wind et al. [41]. A uniplanar dual-mode instrument would also eliminate many of the issues associated with sequential optical-MR microscopy [42], particularly for dynamic time-series experiments. Combining the spatiotemporal resolution of light microscopy with the tissue penetration and unique image information of MR microscopy is a potentially attractive approach for biological imaging applications. Consequently, development of a dual-mode variant of the instrument described here is a near-term priority for this project.

5. Conclusions

We have demonstrated that an efficient uniplanar gradient set can be constructed with sufficient gradient-sample thermal control to allow time-course imaging experiments in sensitive organisms such as developing embryos. Although not a general-purpose instrument, this design is appropriate for high-resolution serial studies of living, opaque organisms in horizontal bore magnets.

Acknowledgments

References

[1] J.M. Tyszka, S.E. Fraser, R.E. Jacobs, Magnetic resonance microscopy: recent advances and applications, Curr. Opin. Biotechnol. 16 (1) (2005) 93–99.
[2] S.C. Lee, K. Kim, J. Kim, S. Lee, J. Han Yi, S.W. Kim, K.S. Ha, C. Cheong, One micrometer resolution NMR microscopy, J. Magn. Reson. 150 (2) (2001) 207–213.
[3] B.R. Smith, E. Linney, D.S. Huff, G.A. Johnson, Magnetic resonance microscopy of embryos, Comput. Med. Imaging Graph. 20 (6) (1996) 483–490.
[4] G.A. Johnson, H. Benveniste, R.D. Black, L.W. Hedlund, R.R. Maronpot, B.R. Smith, Histology by magnetic resonance microscopy, Magn. Reson. Q 9 (1) (1993) 1–30.
[5] C. Papan, B. Boulat, S.S. Velan, S.E. Fraser, R.E. Jacobs, Two-dimensional and three-dimensional time-lapse microscopic magnetic resonance imaging of Xenopus gastrulation movements using intrinsic tissue-specific contrast, Dev. Dyn. 236 (2) (2007) 494–501.
[6] C. Papan, B. Boulat, S.S. Velan, S.E. Fraser, R.E. Jacobs, Time-lapse tracing of mitotic cell divisions in the early *Xenopus* embryo using microscopic MRI, Dev. Dyn. 235 (11) (2006) 3059–3062.
[7] E.M. Shapiro, S. Skrtic, K. Sharer, J.M. Hill, C.E. Dunbar, A.P. Koretsky, MRI detection of single particles for cellular imaging, Proc. Natl. Acad. Sci. USA 101 (30) (2004) 10901–10906.
[8] Y. Matsuda, S. Utsuzawa, T. Kurimoto, T. Haishi, Y. Yamazaki, K. Kose, I. Anno, M. Marutani, Super-parallel MR microscope, Magn. Reson. Med. 50 (1) (2003) 183–189.
[9] M. Dhenain, S.W. Ruffins, R.E. Jacobs, Three-dimensional digital mouse atlas using high-resolution MRI, Dev. Biol. 232 (2) (2001) 458–470.
[10] A.Y. Louie, M.M. Huber, E.T. Ahrens, U. Rothbacher, R. Moats, R.E. Jacobs, S.E. Fraser, T.J. Meade, In vivo visualization of gene expression using magnetic resonance imaging, Nat. Biotechnol. 18 (3) (2000) 321–325.
[11] J.M. Tyszka, C. Readhead, E.L. Bearer, R.G. Pautler, R.E. Jacobs, Statistical diffusion tensor histology reveals regional dysmyelination effects in the shiverer mouse mutant, Neuroimage 29 (4) (2006) 1058–1065.
[12] N. Kovacevic, J.T. Henderson, E. Chan, N. Lifshitz, J. Bishop, A.C. Evans, R.M. Henkelman, X.J. Chen, A three-dimensional MRI atlas of the mouse brain with estimates of the average and variability, Cereb. Cortex 15 (5) (2005) 639–645.
[13] A. MacKenzie-Graham, E.F. Lee, I.D. Dinov, M. Bota, D.W. Shattuck, S. Ruffins, H. Yuan, F. Konstantinidis, A. Pitiot, Y. Ding, G. Hu, R.E. Jacobs, A.W. Toga, A multimodal, multidimensional atlas of the C57BL/6J mouse brain, J. Anat. 204 (2) (2004) 93–102.
[14] G.A. Johnson, G.P. Cofer, S.L. Gewalt, L.W. Hedlund, Morphologic phenotyping with MR microscopy: the visible mouse, Radiology 222 (3) (2002) 789–793.
[15] B. Chronik, A. Alejski, B.K. Rutt, Design and fabrication of a three-axis multilayer gradient coil for magnetic resonance microscopy of mice, Magma 10 (2) (2000) 131–146.
[16] E.A. Jones, D. Crotty, P.M. Kulesa, C.W. Waters, M.H. Baron, S.E. Fraser, M.E. Dickinson, Dynamic in vivo imaging of postimplantation mammalian embryos using whole embryo culture, Genesis 34 (4) (2002) 228–235.
[17] H. Liu, An efficient geometric image distortion correction method for a biplanar planar gradient coil, Magma 10 (2) (2000) 75–79.
[18] E.C. Caparelli, D. Tomasi, H. Panepucci, Shielded biplanar gradient coil design, J. Magn. Reson. Imaging 9 (5) (1999) 725–731.
[19] D. Tomasi, E.C. Caparelli, H. Panepucci, B. Foerster, Fast optimization of a biplanar gradient coil set, J. Magn. Reson. 140 (2) (1999) 325–339.
[20] G.B. Williams, B.J. Fisher, C.L. Huang, T.A. Carpenter, L.D. Hall, Design of biplanar gradient coils for magnetic resonance imaging of the human torso and limbs, Magn. Reson. Imaging 17 (5) (1999) 739–754.
[21] H. Liu, C.L. Truwit, True energy-minimal and finite-size biplanar gradient coil design for MRI, IEEE Trans. Med. Imaging 17 (5) (1998) 826–830.
[22] B.J. Fisher, N. Dillon, T.A. Carpenter, L.D. Hall, Design of a biplanar gradient coil using a genetic algorithm, Magn. Reson. Imaging 15 (3) (1997) 369–376.
[23] B. Aksel, L. Marinelli, B.D. Collick, C. Von Morze, P.A. Bottomley, C.J. Hardy, Local planar gradients with order-of-magnitude strength and speed advantage, Magn. Reson. Med. 58 (1) (2007) 134–143.
[24] R. Lemdiasov, R. Ludwig, M. Brevard, C. Ferris, Design and implementation of a uniplanar gradient field coil for magnetic resonance imaging, Concepts Magn. Reson. B Magn. Reson. Eng. 20B (1) (2004) 17–29.
[25] F.A. Shi, R. Ludwig, Two- and three-dimensional numerical analysis of gradient and parasitic gradient fields of a three-channel surface gradient coil for magnetic resonance imaging, IEEE Trans. Magn. 32 (1) (1996) 195–207.
[26] F. Shi, L.L. Latour, R. Ludwig, C.H. Sotak, A new design for a three-channel surface gradient coil employing a three-dimensional finite element model, Magn. Reson. Med. 35 (4) (1996) 596–605.
[27] Z.H.J.H.Y. Cho, Planar surface gradient coil, Concepts Magn. Reson. 7 (2) (1995) 95–114.
[28] Z.H. Cho, J.H. Yi, A novel type of surface gradient coil, J. Magn. Reson. 94 (1991) 471–485.
[29] S.J. Dodd, C. Ho, Short planar gradient coils for MR microscopy using concentric return paths, J. Magn. Reson. 156 (1) (2002) 1–9.
[30] R.A. Lemdiasov, R. Ludwig, A stream function method for gradient coil design, Concepts Magn. Reson. B Magn. Reson. Eng. 26B (1) (2005) 67–80.
[31] F.N. Fritsch, R.E. Carlson, Monotone piecewise cubic interpolation, Siam J. Numer. Anal. 17 (2) (1980) 238–246.
[32] R. Turner, A target field approach to optimal coil design, J. Phys. D Appl. Phys. 19 (8) (1986) L147–L151.

[33] D. Tomasi, Stream function optimization for gradient coil design, Mag. Reson. Med. 45 (3) (2001) 505–512.

[34] J.M. Tyszka, Y. Kee, R.E. Jacobs, M. Bronner-Fraser, S.E. Fraser, In Vivo 4D Magnetic Resonance Microscopy of Neurulation and Somitogenesis in Amphibian Embryos, Toronto, Canada, 2006, p. 2008.

[35] J. Ashburner, K.J. Friston, Voxel-based morphometry – the methods, Neuroimage 11 (6 Pt. 1) (2000) 805–821.

[36] C. Papan, S.S. Velan, S.E. Fraser, R.E. Jacobs, 3D time-lapse analysis of *Xenopus* gastrulation movements using mu MRI, Dev. Biol. 235 (1) (2001) 189.

[37] J. Jovicich, S. Czanner, D. Greve, E. Haley, A. van der Kouwe, R. Gollub, D. Kennedy, F. Schmitt, G. Brown, J. Macfall, B. Fischl, A. Dale, Reliability in multi-site structural MRI studies: effects of gradient non-linearity correction on phantom and human data, Neuroimage 30 (2) (2006) 436–443.

[38] D.A. Seeber, J.H. Hoftiezer, W.B. Daniel, M.A. Rutgers, C.H. Pennington, Triaxial magnetic field gradient system for microcoil magnetic resonance imaging, Rev. Sci. Instrum. 71 (11) (2000) 4263–4272.

[39] S.J. Dodd, H. Chien, Short planar gradient coils for MR microscopy using concentric return paths, J. Mag. Reson. 156 (1) (2002) 1–9.

[40] S.C. Lee, D. Mietchen, J.H. Cho, Y.S. Kim, C. Kim, K.S. Hong, C. Lee, D. Kang, W. Lee, C. Cheong, In vivo magnetic resonance microscopy of differentiation in *Xenopus* laevis embryos from the first cleavage onwards, Differentiation 75 (1) (2007) 84–92.

[41] R.A. Wind, K.R. Minard, G.R. Holtom, P.D. Majors, E.J. Ackerman, S.D. Colson, D.G. Cory, D.S. Daly, P.D. Ellis, N.F. Metting, C.I. Parkinson, J.M. Price, X.W. Tang, An integrated confocal and magnetic resonance microscope for cellular research, J. Magn. Reson. 147 (2) (2000) 371–377.

[42] P.M. Glover, R.W. Bowtell, G.D. Brown, P. Mansfield, A microscope slide probe for high resolution imaging at 11.7 Tesla, Magn. Reson. Med. 31 (4) (1994) 423–428.